


Topological multiband s -wave superconductivity in coupled multifold fermionsChanghee Lee,¹ Chiho Yoon¹,¹ Taehyeok Kim,¹ Suk Bum Chung^{1,2,3,4,*} and Hongki Min^{1,†}¹*Department of Physics and Astronomy, Seoul National University, Seoul 08826, Korea*²*Department of Physics, University of Seoul, Seoul 02504, Korea*³*Natural Science Research Institute, University of Seoul, Seoul 02504, Korea*⁴*School of Physics, Korea Institute for Advanced Study, Seoul 02455, Korea* (Received 10 May 2021; revised 14 December 2021; accepted 15 December 2021; published 29 December 2021)

We study three-dimensional time-reversal-invariant topological superconductivity in noncentrosymmetric materials such as RhSi, CoSi, and AlPt which host coupled multifold nodes energetically split by the spin-orbit coupling at the same time-reversal-invariant momentum (TRIM). The topological superconductivity arises from the $s_+ \oplus s_-$ gap function, which is \mathbf{k} independent, but with opposite signs for the two nodes split at the same TRIM. We consider various electron-electron interactions in the tight-binding model for RhSi and find that the topological superconducting phase supporting a surface Majorana cone and topological nodal rings is favored in a wide range of interaction parameters.

DOI: [10.1103/PhysRevB.104.L241115](https://doi.org/10.1103/PhysRevB.104.L241115)

Introduction. Majorana particles on superconductors have drawn widespread attention as an avenue to topological quantum computation [1–5], and this can be attributed to their characteristic non-Abelian vortex exchange statistics [6–8]. The majority of experimental search for the Majorana zero modes (MZMs) in condensed matter physics has been based on proposals to realize them in a heterostructure. Examples include the semiconductor nanowire [9–13], the ferromagnetic atomic chain [14], and the topological insulator [15,16] in proximity to a conventional superconductor.

Besides these heterostructures, the development of topological band theory [17–19] has demonstrated that topological materials could exhibit topological superconductivity (TSC) with Majorana boundary modes due to the novel interplay between the unique electronic structures and interactions [20–25]. Recent research has been devoted to understanding the interplay and the resulting TSC in Weyl/Dirac semimetals [26–29] and Luttinger semimetals [30,31].

The recently discovered topological semimetals with unconventional multifold fermions [32] also provide an ideal platform for studying the effects of interactions in the unique electronic structures, especially TSC. In a family of candidate materials with the B20 crystal structure [33,34] such as RhSi, CoSi, and AlPt, the topological features of the electronic structure such as the long surface Fermi arcs have been observed [35–41]. However, some qualitative band structure features of this class of candidate materials have not been included in the existing studies on the interacting multifold fermions [42–46]. Many of them studied isolated multifold fermions at a single time-reversal-invariant momentum (TRIM) and it has not been considered that two types of multifold fermions lie at slightly different energy levels on the

same TRIM. Thus, the possibility of the multiband characteristics to manifest in the superconductivity [47–50] has been overlooked.

In this Letter, we study a possible time-reversal-invariant (TRI) TSC arising from the coupled structure of multifold fermions at TRIMs in a representative multifold fermion system, RhSi. We find that the electronic structure of coupled multifold fermions can give rise to a robust combination of the fully gapped TRI TSC around the coupled nodes at Γ and the nodal TSC around another TRIM, which arises from the \mathbf{k} -independent intranodal pairing gap at each TRIM with opposite signs between the two nodes at the same TRIM; we shall call this the “ $s_+ \oplus s_-$ gap function.”

Low-energy effective model. To study the electronic structure of RhSi, we adopt the tight-binding (TB) model proposed in Ref. [35] [see Sec. I of the Supplemental Material (SM) [51] for the details]. Figure 1(a) shows the TB band structure of RhSi and the first Brillouin zone (BZ) along with the surface BZ (SBZ) on the (001) plane. At Γ , fourfold and twofold nodal points are found around the zero energy corresponding to the (pseudo)spin- $\frac{3}{2}$ Rarita-Schwinger-Weyl (RSW) fermion and spin- $\frac{1}{2}$ Kramer-Weyl (KW) fermion, respectively. Additionally, there are sixfold and twofold nodal points at R which are equivalent to doubly degenerate spin-1 [39,53–55] and spin-0 systems, respectively. As shown in Fig. 1(a), the Fermi level of RhSi lies around the fourfold nodal point at Γ and the energy bands crossing the Fermi level emanate from the multifold nodal points at Γ and R.

We first investigate a low-energy effective model around Γ . Up to first order in \mathbf{k} , the electronic band structure near the two nodal points at Γ is described by the following Hamiltonian:

$$H_{\mathbf{k}}^{3/2 \oplus 1/2} = \begin{pmatrix} H_{\mathbf{k}}^{(3/2)} & T_{\Gamma, \mathbf{k}} \\ T_{\Gamma, \mathbf{k}}^{\dagger} & H_{\mathbf{k}}^{(1/2)} - m_{\Gamma} I_2 \end{pmatrix}, \quad (1)$$

*sbchung0@uos.ac.kr

†hmin@snu.ac.kr

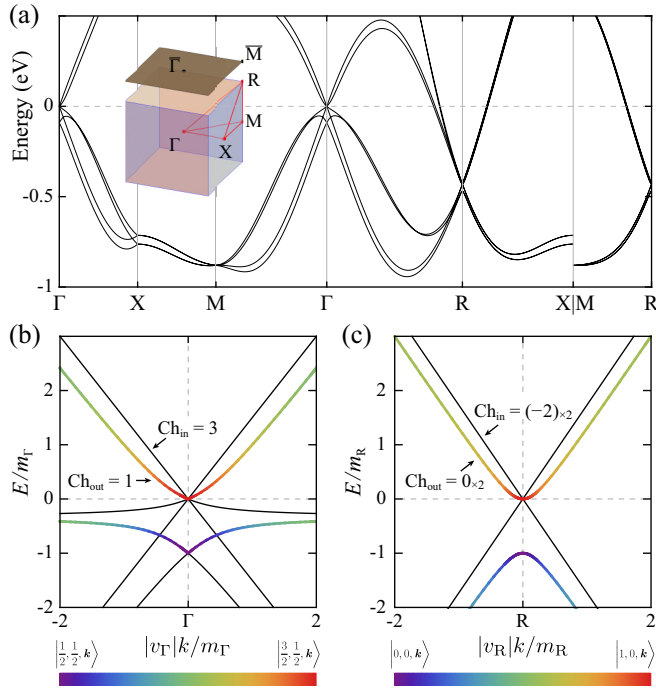


FIG. 1. (a) Band structure of RhSi along the high-symmetry lines in the BZ. The BZ and the (001) SBZ are shown in the inset. (b),(c) The band structure of the continuum model near the nodal points at Γ (R). The ratio of the wave function magnitude between $|\frac{3}{2}, \frac{1}{2}, \hat{\mathbf{k}}\rangle$ and $|\frac{1}{2}, \frac{1}{2}, \hat{\mathbf{k}}\rangle$ ($|1, 0, \hat{\mathbf{k}}\rangle$ and $|0, 0, \hat{\mathbf{k}}\rangle$) is illustrated by different colors. For the bands with $E > 0$, Ch_{in} and Ch_{out} are the Chern numbers carried by the inner and outer FSSs, respectively, and $\times 2$ in the subscript indicates double degeneracy.

where $H_{\mathbf{k}}^{(3/2)} = v_{\Gamma} \mathbf{k} \cdot \mathbf{S}^{(3/2)}$ and $H_{\mathbf{k}}^{(1/2)} = 2v_{\Gamma} \mathbf{k} \cdot \mathbf{S}^{(1/2)}$ describe the RSW and KW fermions, respectively, with the spin- s matrices $S_i^{(s)}$ satisfying $\mathbf{S}^{(s)2} = s(s+1)$. Here, v_{Γ} and $2v_{\Gamma}$ are the Fermi velocities of RSW and KW fermions, respectively. In the RhSi family, they originate from spin-independent inversion-breaking hoppings. We denote the eigenstates of $H_{\mathbf{k}}^{(s)}$ by $|s, h_z, \hat{\mathbf{k}}\rangle$, where s and h_z are the total angular momentum and the helicity eigenvalue, respectively. We assume $v_{\Gamma} > 0$ without loss of generality. The two nodal points are energetically separated by m_{Γ} and coupled by $T_{\Gamma, \mathbf{k}} = \frac{v_{\Gamma} k}{\sqrt{2}} (|\frac{3}{2}, \frac{1}{2}, \hat{\mathbf{k}}\rangle \langle \frac{1}{2}, \frac{1}{2}, \hat{\mathbf{k}}| + |\frac{3}{2}, -\frac{1}{2}, \hat{\mathbf{k}}\rangle \langle \frac{1}{2}, -\frac{1}{2}, \hat{\mathbf{k}}|)$.

When the Fermi level lies above the fourfold nodal point, two bands of $H_{\mathbf{k}}^{3/2 \oplus 1/2}$ cross the Fermi level as shown in Fig. 1(b). Their eigenstates are given by

$$\begin{aligned} |\Gamma, \text{in}, \mathbf{k}\rangle &= |\frac{3}{2}, \frac{3}{2}, \hat{\mathbf{k}}\rangle, \\ |\Gamma, \text{out}, \mathbf{k}\rangle &= \cos \theta_{\Gamma, \mathbf{k}} |\frac{3}{2}, \frac{1}{2}, \hat{\mathbf{k}}\rangle + \sin \theta_{\Gamma, \mathbf{k}} |\frac{1}{2}, \frac{1}{2}, \hat{\mathbf{k}}\rangle, \end{aligned} \quad (2)$$

where $\theta_{\Gamma, \mathbf{k}} = \tan^{-1} \sqrt{\frac{f_{\Gamma, \mathbf{k}} - e_{\Gamma, \mathbf{k}}}{f_{\Gamma, \mathbf{k}} + e_{\Gamma, \mathbf{k}}}}$ with $e_{\Gamma, \mathbf{k}} = m_{\Gamma} - v_{\Gamma} k/2$ and $f_{\Gamma, \mathbf{k}} = \sqrt{e_{\Gamma, \mathbf{k}}^2 + 2v_{\Gamma}^2 k^2}$. Here, ‘‘in’’ and ‘‘out’’ represent the inner and outer Fermi surface sheets (FSSs), respectively. Note that the outer FSS mainly consists of the $h_z = \frac{1}{2}$ branch of the RSW fermion in the limit $v_{\Gamma} k \ll m_{\Gamma}$, while the portion of the KW fermion $|\frac{1}{2}, \frac{1}{2}, \hat{\mathbf{k}}\rangle$ increases to $\frac{2}{3}$ in the opposite limit. In Fig. 1(b), the bands composed of the $h_z = \frac{1}{2}$ branches of the

RSW and KW fermions are colored according to their ratio. A FSS surrounding a multifold fermion carries a quantized Chern number $2h_z$ when each eigenstate on the FSS is a superposition of $|s, h_z, \hat{\mathbf{k}}\rangle$'s with the same h_z . Thus, the inner and outer FSSs carry the Chern numbers 3 and 1, respectively.

The low-energy effective model near R is analogous to that near Γ . Up to first order in \mathbf{k} , the electronic band structure around sixfold and twofold nodal points at R is described by two copies of coupled spin-1 and spin-0 fermions $H_{\mathbf{k}}^{1 \oplus 0} \oplus H_{\mathbf{k}}^{1 \oplus 0}$, where $H_{\mathbf{k}}^{1 \oplus 0}$ is given by

$$H_{\mathbf{k}}^{1 \oplus 0} = \begin{pmatrix} H_{\mathbf{k}}^{(1)} & T_{\mathbf{R}, \mathbf{k}} \\ T_{\mathbf{R}, \mathbf{k}}^{\dagger} & H_{\mathbf{k}}^{(0)} \end{pmatrix} = \begin{pmatrix} -v_{\mathbf{R}} \mathbf{k} \cdot \mathbf{S}^{(1)} & T_{\mathbf{R}, \mathbf{k}} \\ T_{\mathbf{R}, \mathbf{k}}^{\dagger} & -m_{\mathbf{R}} \end{pmatrix}, \quad (3)$$

where the two nodal points are coupled by $T_{\mathbf{R}, \mathbf{k}} = v_{\mathbf{R}} k |1, 0, \hat{\mathbf{k}}\rangle \langle 0, 0, \hat{\mathbf{k}}|$. Here, $v_{\mathbf{R}} > 0$ since the Nielsen-Ninomiya theorem [56] requires $v_{\Gamma} v_{\mathbf{R}} > 0$.

As shown in Fig. 1(c), two bands of $H_{\mathbf{k}}^{1 \oplus 0}$ cross the Fermi level when it lies above the sixfold nodal point, whose eigenstates are given by

$$\begin{aligned} |\mathbf{R}, \text{in}, \mathbf{k}\rangle &= |1, -1, \hat{\mathbf{k}}\rangle, \\ |\mathbf{R}, \text{out}, \mathbf{k}\rangle &= \cos \theta_{\mathbf{R}, \mathbf{k}} |1, 0, \hat{\mathbf{k}}\rangle + \sin \theta_{\mathbf{R}, \mathbf{k}} |0, 0, \hat{\mathbf{k}}\rangle, \end{aligned} \quad (4)$$

where $\theta_{\mathbf{R}, \mathbf{k}} = \tan^{-1} (\sqrt{\frac{f_{\mathbf{R}, \mathbf{k}} - m_{\mathbf{R}}}{f_{\mathbf{R}, \mathbf{k}} + m_{\mathbf{R}}}})$ with $f_{\mathbf{R}, \mathbf{k}} = \sqrt{m_{\mathbf{R}}^2 + 4v_{\mathbf{R}}^2 k^2}$. Equation (4) is very similar to Eq. (2). The Chern numbers carried by the inner and outer FSSs are -2 and 0 , respectively, for each copy. Then the total Chern number of the Fermi surface around R is -4 compensating the Chern numbers from the FSSs around the RSW and KW nodes at Γ .

TSC from $s_+ \oplus s_-$ pairings. Considering the two coupled nodal points at Γ or R, TRI TSC can arise even from the simplest \mathbf{k} -independent gap functions represented by a direct sum of two trivial matrices respecting all the spatial symmetries of the system. Besides the trivial gap function, the multinodal nature of each TRIM in the system allows the $s_+ \oplus s_-$ gap functions:

$$\Delta_{\pm}^{\Gamma} = \begin{pmatrix} I_4 & \\ & -2I_2 \end{pmatrix}, \quad \Delta_{\pm}^{\mathbf{R}} = \begin{pmatrix} I_3 & \\ & -3I_1 \end{pmatrix}, \quad (5)$$

where I_{2s+1} acts on spin- s fermions. $\Delta_{\pm}^{\Gamma(\mathbf{R})}$ looks like the trivial gap function if we just focus on one of the two nodal points at Γ (R), but the sign of the gap function on each nodal point is opposite. Note that the $s_+ \oplus s_-$ gap functions indicate spin-triplet pairing (see Sec. II of the SM [51]). We shall show later that, for generic electron-electron interactions, the TRI solution of the linearized gap equation can be written as

$$\begin{aligned} \Delta_{\Gamma}(\beta_{\Gamma}) &= \alpha_{\Gamma} (\Delta_{\pm}^{\Gamma} \cos \beta_{\Gamma} + I_6 \sin \beta_{\Gamma}), \\ \Delta_{\mathbf{R}}(\beta_{\mathbf{R}}) &= \alpha_{\mathbf{R}} (\Delta_{\pm}^{\mathbf{R}} \cos \beta_{\mathbf{R}} + I_4 \sin \beta_{\mathbf{R}}), \end{aligned} \quad (6)$$

near Γ and R, respectively. Here, $\alpha_{\Gamma(\mathbf{R})}$ corresponds to the overall magnitude of the gap function and $\beta_{\Gamma(\mathbf{R})} \in [-\frac{\pi}{2}, \frac{\pi}{2}]$ parametrizes the ratio between the trivial gap function and the $s_+ \oplus s_-$ gap function. We assume $\alpha_{\Gamma}, \alpha_{\mathbf{R}} > 0$ here (see Sec. III of the SM [51] for more general cases).

To understand the topological nature of the superconducting phase with the gap function $\Delta_{\Gamma}(\beta_{\Gamma})$, we first focus on the multifold fermions at Γ and study the Bogliubov–de Gennes

(BdG) Hamiltonian $\hat{H}_{\text{BdG}} = \frac{1}{2} \sum_{\mathbf{k}} \hat{\Psi}_{\mathbf{k}}^\dagger H_{\text{BdG}}(\mathbf{k}) \hat{\Psi}_{\mathbf{k}}$ with

$$H_{\text{BdG},\Gamma}(\mathbf{k}) = \begin{pmatrix} H_{\mathbf{k}}^{3/2\oplus 1/2} - \mu_\Gamma & \Delta_\Gamma(\beta_\Gamma) \\ \Delta_\Gamma(\beta_\Gamma) & \mu_\Gamma - H_{\mathbf{k}}^{3/2\oplus 1/2} \end{pmatrix}. \quad (7)$$

Here, $\hat{\Psi}_{\mathbf{k}} = (\hat{C}_{\mathbf{k}}^\dagger, \hat{C}_{-\mathbf{k}}^T \gamma)$ is a spinor with the creation (destruction) operator $\hat{C}_{\mathbf{k}}^\dagger$ ($\hat{C}_{\mathbf{k}}$) for electrons of the $H_{\mathbf{k}}^{3/2\oplus 1/2}$ and $\gamma = \exp[-i\pi S_y^{(3/2)}] \oplus \exp[-i\pi S_y^{(1/2)}]$ is the unitary part of the time-reversal operator, and μ_Γ is the Fermi level measured from the fourfold nodal point.

In the weak pairing limit with α_Γ much smaller than the energy separation between the bands near the Fermi level, the BdG spectrum and its topology are largely determined by the intraband gap functions given by

$$\begin{aligned} \delta_{\Gamma,\text{in}} &\equiv \langle \Gamma, \text{in}, \mathbf{k} | \Delta_\Gamma(\beta_\Gamma) | \Gamma, \text{in}, \mathbf{k} \rangle |_{\mathbf{k}=k_{\text{F},\text{in}}} \\ &= \alpha_\Gamma \cos \beta_\Gamma (\tan \beta_\Gamma + 1), \\ \delta_{\Gamma,\text{out}} &\equiv \langle \Gamma, \text{out}, \mathbf{k} | \Delta_\Gamma(\beta_\Gamma) | \Gamma, \text{out}, \mathbf{k} \rangle |_{\mathbf{k}=k_{\text{F},\text{out}}} \\ &\approx \alpha_\Gamma \cos \beta_\Gamma [\tan \beta_\Gamma - g_\Gamma(\mu_\Gamma/m_\Gamma)], \end{aligned} \quad (8)$$

with $g_\Gamma(x) = \frac{3x^2 - 2x - 1}{3x^2 + 2x + 1}$, while the interband gap functions can be treated perturbatively. The approximation in Eq. (8) is valid as long as α_Γ is sufficiently small compared to $|3\mu_\Gamma + m_\Gamma|$.

The key insight here is that μ_Γ determines the sign of $\delta_{\Gamma,\text{out}}$ when $|\beta_\Gamma| < \pi/4$. This is most apparent in the case of $\beta_\Gamma = 0$ in Eq. (6) from the wave function character in Eq. (2). Because $\Delta_\Gamma(0) \propto \Delta_\pm^\Gamma$ in Eq. (6), $\delta_{\Gamma,\text{out}} > 0$ for small $\mu_\Gamma > 0$ since the outer FSS is mainly composed of the RSW fermion. As μ_Γ is increased, however, so does the composition of the KW fermion in the outer FSS, and Δ_\pm^Γ gives $\delta_{\Gamma,\text{out}} < 0$. Hence, the variation in the wave-function character switches the sign of $\delta_{\Gamma,\text{out}}$.

In the same manner, we define $\delta_{\text{R},\text{in}}$ and $\delta_{\text{R},\text{out}}$, which have the same form as those in Eq. (8) but with $g_{\text{R}}(x) = \frac{2x-1}{2x+1}$, and find that the sign of $\delta_{\text{R},\text{out}}$ also can be flipped by adjusting $\mu_{\text{R}} > 0$ when $|\beta_{\text{R}}| < \pi/4$.

Phase diagrams in Figs. 2(a) and 2(b) summarize the topological phases at Γ and R, respectively. When the whole BdG spectrum is gapped, a winding number $w_{3\text{D}}$ determines the topology and the number of helical MZMs on the SBZ [19]. However, as explained below, a TSC with nodal rings (NRs) around R can appear for large μ_{R} . In this case, the presence/absence of a MZM at $\bar{\Gamma}$ can be determined by a winding number $w_{1\text{D}}$ [57]. Hence, we use a pair of winding numbers ($w_{3\text{D}}, w_{1\text{D}}$) to characterize the topology of each region in the phase diagrams.

In the weak pairing limit, $w_{3\text{D}}$ is expressed as [18]

$$w_{3\text{D}} = \frac{1}{2} \sum_n \text{sgn}(\delta_n) \text{Ch}_n, \quad (9)$$

where Ch_n is the Chern number of the n th FSS. We break $w_{3\text{D}}$ into $w_{3\text{D},\Gamma}$ and $w_{3\text{D},\text{R}}$ according to the centers of FSSs. For $w_{3\text{D},\Gamma}$, we expect it to be ± 2 or $+1$, and the latter occurs only when $\delta_{\Gamma,\text{out}} \delta_{\Gamma,\text{in}} < 0$. Meanwhile, $w_{3\text{D},\text{R}} = -2 \text{sgn}(\delta_{\text{R},\text{in}})$ is always even. Consequently, $w_{3\text{D}}$ is odd whenever $\delta_{\Gamma,\text{out}} \delta_{\Gamma,\text{in}} < 0$, and we expect at least one topologically protected MZM at $\bar{\Gamma}$ on SBZ.

Unlike $\delta_{\Gamma,\text{out}}$, the sign flip of $\delta_{\text{R},\text{out}}$ with μ_{R} has no effect on $w_{3\text{D}}$ since $\text{Ch}_{\text{R},\text{out}} = 0$. Nevertheless, it can lead to a nodal

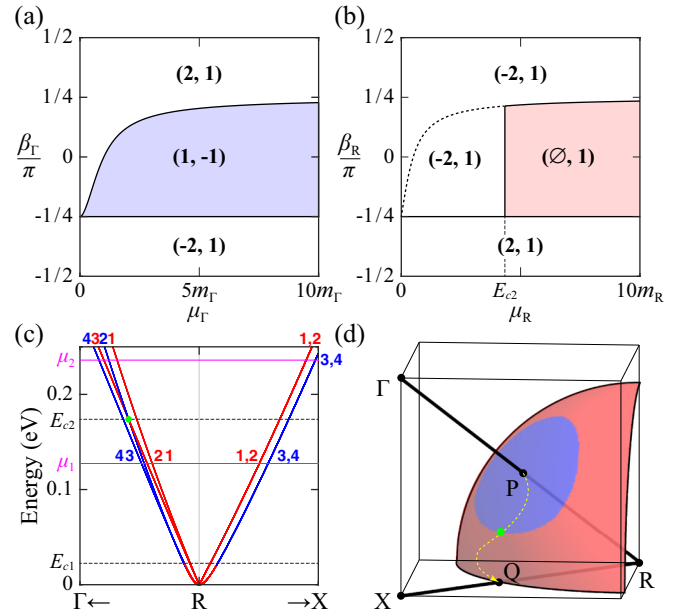


FIG. 2. (a),(b) Phase diagram of the TSC in RhSi with respect to β_Γ and μ_Γ with $\alpha_\Gamma > 0$ (β_{R} and μ_{R} with $\alpha_{\text{R}} > 0$). A pair of winding numbers ($w_{3\text{D},\Gamma(\text{R})}$, $w_{1\text{D},\Gamma(\text{R})}$) on each region characterizes the topology of the superconducting phase. $w_{3\text{D},\text{R}} = \emptyset$ indicates the TSC with NRs in the bulk BdG spectrum. The dashed line represents $\mu_{\text{R}} = E_{c1}(\beta_{\text{R}})$ on which the superconducting gap closes/reopens without changing $w_{3\text{D}}$ and $w_{1\text{D}}$. (c) The band structure around R above the sixfold nodal point colored in red (blue) for positive (negative) $\delta_{\text{R},n}$. The four bands are labeled as $n = 1, 2, 3, 4$ in the order of closeness to R. (d) The FSS formed by band 2 at $\mu = \mu_2$, colored in the same manner as (c).

TSC in RhSi for sufficiently large μ_{R} , around which the band structure can be understood by considering the anisotropic \mathbf{k} -quadratic correction to $H_{\mathbf{k}}^{1\oplus 0} \oplus H_{\mathbf{k}}^{1\oplus 0}$. Breaking the artificial isotropy of $H_{\mathbf{k}}^{1\oplus 0} \oplus H_{\mathbf{k}}^{1\oplus 0}$ in \mathbf{k} , it modifies the band structure in Fig. 1(c) in two ways. First, there appear band crossings along the $\text{R}\bar{\Gamma}$ lines because of the symmetry-enforced band connectivity [58]. Second, the double degeneracy of the model in Eq. (3) is lifted in generic momenta in BZ except on $k_{x,y,z} = \pi$ planes due to the local Kramers theorem from the twofold screw symmetries and the time-reversal symmetry [35].

Both effects are clearly shown in Fig. 2(c). The bands crossing the Fermi level $\mu_{\text{R}} > 0$ are labeled by $n = 1, 2, 3, 4$ in the order of closeness to R, and the color represents the sign of $\delta_{\text{R},n}$ for $\beta_{\text{R}} = 0$ in Eq. (6). As explained, the signs of $\delta_{\text{R},3}$ and $\delta_{\text{R},4}$ are flipped as μ_{R} is raised over $E_{c1}(\beta_{\text{R}}) = \frac{m_{\text{R}}}{2} \left(\frac{1+\tan \beta_{\text{R}}}{1-\tan \beta_{\text{R}}} \right)$ at which $g_{\text{R}}(\mu_{\text{R}}/m_{\text{R}}) = \tan \beta_{\text{R}}$. For $\beta_{\text{R}} = 0$, $E_{c1} = m_{\text{R}}/2$. The switched signs are maintained for the higher energies.

The BdG spectrum around R remains gapped until μ_{R} reaches the band crossing energy E_{c2} . For $\mu_{\text{R}} > E_{c2}$, however, topological NRs in the BdG spectrum appear because the interchange of wave functions between bands 2 and 3 at the band crossing on the $\text{R}\bar{\Gamma}$ line makes the signs of $\delta_{\text{R},2(3)}$ on the $\text{R}\bar{\Gamma}$ line and on the $k_{x,y,z} = \pi$ planes opposite. Suppose P (Q) to be a point where the FSS of band 2 and the $\text{R}\bar{\Gamma}$ line (RX line) meet as shown in Fig. 2(d). Since $\delta_{\text{P}} \delta_{\text{Q}} < 0$, there exists at least a point where the gap function becomes zero for any

path between P and Q on the FSS. As a result, a ring with $\delta_{R,2} = 0$ wrapping the $R\Gamma$ line appears on the FSS of band 2. For the same reason, another NR is found on the FSS of band 3. The stability of NRs is guaranteed by the one-dimensional (1D) winding number for the AIII class evaluated along a loop enclosing the ring [59]. The rings from bands 2 and 3 have opposite winding numbers of unit magnitude (see Sec. IV of the SM [51]).

Even in the presence of NRs around R, a MZM at $\bar{\Gamma}$ is still protected by w_{1D} evaluated along a TRI loop \mathcal{L} connecting Γ with another TRIM that is projected to $\bar{\Gamma}$ on the SBZ without intersecting with NRs in the BZ [59]. In the weak pairing limit, w_{1D} can be easily evaluated from [18]

$$w_{1D} = \prod_{n \in \text{FSS}'} \text{sgn}(\delta_n), \quad (10)$$

where FSS' denotes the FSSs which intersect with \mathcal{L} . Note that the four FSSs near R do not contribute to w_{1D} due to the local Kramers degeneracies implying $\delta_{R,2n-1} = \delta_{R,2n}$ for $n = 1, 2$. Thus, a MZM at $\bar{\Gamma}$ is expected for any surfaces of the crystal as long as $\delta_{\Gamma, \text{in}} \delta_{\Gamma, \text{out}} < 0$, which is consistent with the condition in the fully gapped phase.

TSC phase diagram in various interactions. To investigate what kind of interactions realize the $s_+ \oplus s_-$ gap functions, we consider three types of electron-electron interactions:

$$\hat{H}_{\text{int}} = \frac{U}{2} \sum_i \hat{\rho}_i \hat{\rho}_i + \frac{V}{2} \sum_{(i,j)} \hat{\rho}_i \hat{\rho}_j + \frac{J}{2} \sum_{(i,j)} \hat{S}_i \cdot \hat{S}_j. \quad (11)$$

Here, $(\hat{\rho}_i, \hat{S}_i) = (\hat{C}_{i,\uparrow}^\dagger, \hat{C}_{i,\downarrow}^\dagger)(s_0, s)(\hat{C}_{i,\uparrow}, \hat{C}_{i,\downarrow})^T$ with the spin Pauli matrices s . U , V , and J represent the renormalized on-site Coulomb interaction, the nearest-neighbor Coulomb interaction, and the nearest-neighbor (anti)ferromagnetic exchange interaction, respectively [60]. Considering only the time-reversal invariant pairing channels from \hat{H}_{int} respecting spatial symmetries of RhSi, the pairing interaction \hat{H}_{pair} can be expressed as

$$\hat{H}_{\text{pair}} = \sum_{i=0}^8 \frac{U_i}{4} \sum_{k,p} \hat{\Pi}_i(\mathbf{k}) \hat{\Pi}_i^\dagger(\mathbf{p}), \quad (12)$$

where $\hat{\Pi}_i(\mathbf{k}) = \hat{C}_{-k}^T \gamma M_{i,k}^\dagger \hat{C}_k$, and U_i 's are the coupling constants of the pairing channels $\hat{\Pi}_i \hat{\Pi}_i^\dagger$ with $U_0 = U/4$, $U_{1,5} = V - 3J$, and $U_{2,3,4,6,7,8} = V + J$. Here, $M_{i,k}$ are \mathbf{k} -dependent matrices characterizing the pairing channels (see Sec. I of the SM [51]).

Solving the linearized gap equation with \hat{H}_{pair} , the gap function $\Delta(\mathbf{k}) = \sum_{i=0}^8 \Delta_i M_{i,k}$ with the highest transition temperature is obtained. The relationship between $\Delta(\mathbf{k})$ and Eq. (6) can be understood by projecting $\Delta(\mathbf{k})$ to the bases of $H_k^{3/2 \oplus 1/2}$ and $H_k^{1 \oplus 0}$ at Γ and R, respectively. At Γ , $\Delta(\mathbf{k}) \sim (\Delta_0 - \Delta_1)I_6 + (\Delta_2 - \Delta_3)\Delta_{\pm}^\Gamma$, whereas at R, $\Delta(\mathbf{k}) \sim \Delta_0 I_4 + \Delta_4 \Delta_{\pm}^R$ up to the zeroth order in \mathbf{k} . For $U < 0$, the trivial gap function largely prevails. Hence, we focus on $U > 0$.

Figure 3(a) shows the phase diagram in $(V/U, J/U)$ for $U > 0$ at $\mu = \mu_\Gamma = \mu_R - 0.43 \text{ eV} = 1.3m_\Gamma$. In the blue “NR+MZM” region, we find that the $s_+ \oplus s_-$ gap functions are dominant and the resultant TSC exhibits a MZM at $\bar{\Gamma}$ and the NRs near R as shown in Figs. 3(b) and 3(c), respec-

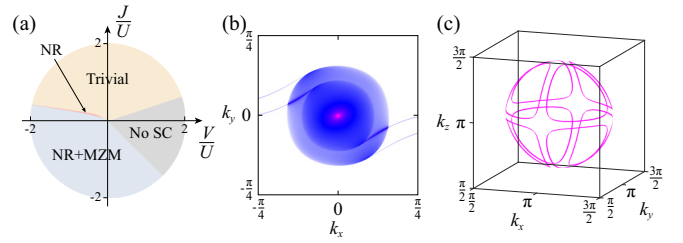


FIG. 3. (a) Phase diagram in $(V/U, J/U)$ at $\mu = 1.3m_\Gamma$ with $U > 0$. “No SC” and “Trivial” mean no superconductivity and the topologically trivial superconducting phase, respectively, whereas “NR” and “MZM” represent the superconducting phases with the NRs around R, and a MZM at $\bar{\Gamma}$, respectively. (b) Surface spectral weight around $\bar{\Gamma}$ at $E = 0$. (c) Nodal rings around R in the BZ.

tively. This region is approximately covered by $V < -J$ with $J < 0$, where the ferromagnetic interaction is stronger than the nearest-neighbor Coulomb interaction. In a narrow region in red at the boundary of the blue region, the TSC with only the NRs from Δ_{\pm}^R appears. The beige region marked by “Trivial” approximately overlaps with $V < 3J$ with $J > 0$, where the topologically trivial superconductivity arises from the spin-singlet pairings due to the antiferromagnetic interaction $J > 0$ in contrast to the “NR+MZM” region. Near the phase boundaries, TSC phases with additional NRs around Γ or R may appear due to a complicated combination of various gap functions (see Sec. V of the SM [51]).

Discussion. The $s_+ \oplus s_-$ gap functions in our work should be distinguished from the momentum-dependent s_{\pm} gap functions usually discussed in iron-based superconductors [61]. We find that an analogous gap function for our system, corresponding to $\alpha_\Gamma \alpha_R < 0$ in Eq. (6) [45,46], is not favored by the electron-electron interaction of Eq. (11) (see Sec. V of the SM [51]).

Regarding the experimental realization, we want to refer to the report on the multigap superconductivity in RhGe [62] whose electronic structure is akin to RhSi. Considering weak ferromagnetism in RhGe, it is expected that the TSC arising from the $s_+ \oplus s_-$ gap functions could be realized by varying its chemical compositions [63]. Also, we expect that our result could be applied to the multigap superconductor BeAu [64–66] in B20 structure as well as other noncentrosymmetric superconductors such as $\text{Li}_2\text{X}_3\text{B}$ ($X = \text{Pd}, \text{Pt}$) [46], PtSb [67], and BaPtP [68] supporting coupled multifold fermions.

The TSC from the $s_+ \oplus s_-$ gap functions can be investigated by probing the bulk and surface properties, respectively. To discern the gap function from the trivial s -wave gap function, magnetic resonance techniques and angle-resolved photoemission spectroscopy can be used to identify the spin state of the gap function and the size of the superconducting gap on each FSS, respectively [69,70]. Regarding the response from the surface, drastic anisotropy in response to magnetic fields could be a smoking gun of the MZMs on the surface [71–73].

Acknowledgments. This work was supported by the National Research Foundation of Korea (NRF) grant funded by the Korea government (MSIT) (Grant No.

2018R1A2B6007837) and Creative-Pioneering Researchers Program through Seoul National University (SNU). C.Y. was supported by NRF of Korea under Grant No. 2016H1A2A1907780 through the Global PhD Fellow-

ship Program. S.B.C. was supported by NRF grants funded by the Korea government (MSIT) (Grant No. 2020R1A2C1007554) and the Ministry of Education (Grant No. 2018R1A6A1A06024977).

-
- [1] J. Alicea, *Rep. Prog. Phys.* **75**, 076501 (2012).
- [2] C. Beenakker, *Annu. Rev. Condens. Matter Phys.* **4**, 113 (2013).
- [3] T. D. Stanescu and S. Tewari, *J. Phys.: Condens. Matter* **25**, 233201 (2013).
- [4] M. Sato and S. Fujimoto, *J. Phys. Soc. Jpn.* **85**, 072001 (2016).
- [5] M. Sato and Y. Ando, *Rep. Prog. Phys.* **80**, 076501 (2017).
- [6] N. Read and D. Green, *Phys. Rev. B* **61**, 10267 (2000).
- [7] L. Fidkowski, X. Chen, and A. Vishwanath, *Phys. Rev. X* **3**, 041016 (2013).
- [8] T. Sanno, S. Miyazaki, T. Mizushima, and S. Fujimoto, *Phys. Rev. B* **103**, 054504 (2021).
- [9] Y. Oreg, G. Refael, and F. von Oppen, *Phys. Rev. Lett.* **105**, 177002 (2010).
- [10] J. D. Sau, R. M. Lutchyn, S. Tewari, and S. Das Sarma, *Phys. Rev. Lett.* **104**, 040502 (2010).
- [11] R. M. Lutchyn, J. D. Sau, and S. Das Sarma, *Phys. Rev. Lett.* **105**, 077001 (2010).
- [12] C.-X. Liu, J. D. Sau, T. D. Stanescu, and S. Das Sarma, *Phys. Rev. B* **96**, 075161 (2017).
- [13] E. Prada, P. San-Jose, M. W. de Moor, A. Geresdi, E. J. Lee, J. Klinovaja, D. Loss, J. Nygård, R. Aguado, and L. P. Kouwenhoven, *Nat. Rev. Phys.* **2**, 575 (2020).
- [14] S. Nadj-Perge, I. K. Drozdov, J. Li, H. Chen, S. Jeon, J. Seo, A. H. MacDonald, B. A. Bernevig, and A. Yazdani, *Science* **346**, 602 (2014).
- [15] L. Fu and C. L. Kane, *Phys. Rev. Lett.* **100**, 096407 (2008).
- [16] L. Fu and C. L. Kane, *Phys. Rev. B* **79**, 161408(R) (2009).
- [17] L. Fu, C. L. Kane, and E. J. Mele, *Phys. Rev. Lett.* **98**, 106803 (2007).
- [18] X. L. Qi, T. L. Hughes, and S. C. Zhang, *Phys. Rev. B* **81**, 134508 (2010).
- [19] C.-K. Chiu, J. C. Y. Teo, A. P. Schnyder, and S. Ryu, *Rev. Mod. Phys.* **88**, 035005 (2016).
- [20] E.-G. Moon, C. Xu, Y. B. Kim, and L. Balents, *Phys. Rev. Lett.* **111**, 206401 (2013).
- [21] I. F. Herbut and L. Janssen, *Phys. Rev. Lett.* **113**, 106401 (2014).
- [22] J. Maciejko and R. Nandkishore, *Phys. Rev. B* **90**, 035126 (2014).
- [23] F. Detassis, L. Fritz, and S. Grubinskas, *Phys. Rev. B* **96**, 195157 (2017).
- [24] S. E. Han, C. Lee, E.-G. Moon, and H. Min, *Phys. Rev. Lett.* **122**, 187601 (2019).
- [25] W. Shi, B. J. Wieder, H. L. Meyerheim, Y. Sun, Y. Zhang, Y. Li, L. Shen, Y. Qi, L. Yang, J. Jena, P. Werner, K. Koepf, S. Parkin, Y. Chen, C. Felser, B. A. Bernevig, and Z. Wang, *Nat. Phys.* **17**, 381 (2021).
- [26] X. Wan, A. M. Turner, A. Vishwanath, and S. Y. Savrasov, *Phys. Rev. B* **83**, 205101 (2011).
- [27] A. A. Burkov and L. Balents, *Phys. Rev. Lett.* **107**, 127205 (2011).
- [28] T. O. Wehling, A. M. Black-Schaffer, and A. V. Balatsky, *Adv. Phys.* **63**, 1 (2014).
- [29] N. P. Armitage, E. J. Mele, and A. Vishwanath, *Rev. Mod. Phys.* **90**, 015001 (2018).
- [30] S. Murakami, N. Nagaosa, and S.-C. Zhang, *Phys. Rev. B* **69**, 235206 (2004).
- [31] T. Kondo, M. Nakayama, R. Chen, J. J. Ishikawa, E. G. Moon, T. Yamamoto, Y. Ota, W. Malaeb, H. Kanai, Y. Nakashima, Y. Ishida, R. Yoshida, H. Yamamoto, M. Matsunami, S. Kimura, N. Inami, K. Ono, H. Kumigashira, S. Nakatsuji, L. Balents, and S. Shin, *Nat. Commun.* **6**, 10042 (2015).
- [32] B. Bradlyn, J. Cano, Z. Wang, M. G. Vergniory, C. Felser, R. J. Cava, and B. A. Bernevig, *Science* **353**, aaf5037 (2016).
- [33] S. Mühlbauer, B. Binz, F. Jonietz, C. Pfleiderer, A. Rosch, A. Neubauer, R. Georgii, and P. Böni, *Science* **323**, 915 (2009).
- [34] D. A. Pshenay-Severin and A. T. Burkov, *Materials* **12**, 2710 (2019).
- [35] G. Chang, S.-Y. Xu, B. J. Wieder, D. S. Sanchez, S.-M. Huang, I. Belopolski, T.-R. Chang, S. Zhang, A. Bansil, H. Lin, and M. Z. Hasan, *Phys. Rev. Lett.* **119**, 206401 (2017).
- [36] Z. Ni, B. Xu, M. Á. Sánchez-Martínez, Y. Zhang, K. Manna, C. Bernhard, J. W. F. Venderbos, F. de Juan, C. Felser, A. G. Grushin, and L. Wu, *npj Quantum Mater.* **5**, 96 (2020).
- [37] D. Rees, K. Manna, B. Lu, T. Morimoto, H. Borrmann, C. Felser, J. E. Moore, D. H. Torchinsky, and J. Orenstein, *Sci. Adv.* **6**, eaba0509 (2020).
- [38] D. S. Sanchez, I. Belopolski, T. A. Cochran, X. Xu, J.-X. Yin, G. Chang, W. Xie, K. Manna, V. Süß, C.-Y. Huang, N. Alidoust, D. Multer, S. S. Zhang, N. Shumiya, X. Wang, G.-Q. Wang, T.-R. Chang, C. Felser, S.-Y. Xu, S. Jia, H. Lin, and M. Z. Hasan, *Nature (London)* **567**, 500 (2019).
- [39] D. Takane, Z. Wang, S. Souma, K. Nakayama, T. Nakamura, H. Oinuma, Y. Nakata, H. Iwasawa, C. Cacho, T. Kim, K. Horiba, H. Kumigashira, T. Takahashi, Y. Ando, and T. Sato, *Phys. Rev. Lett.* **122**, 076402 (2019).
- [40] Z. Rao, H. Li, T. Zhang, S. Tian, C. Li, B. Fu, C. Tang, L. Wang, Z. Li, W. Fan, J. Li, Y. Huang, Z. Liu, Y. Long, C. Fang, H. Weng, Y. Shi, H. Lei, Y. Sun, T. Qian, and H. Ding, *Nature (London)* **567**, 496 (2019).
- [41] N. B. M. Schröter, D. Pei, M. G. Vergniory, Y. Sun, K. Manna, F. de Juan, J. A. Krieger, V. Süß, M. Schmidt, P. Dudin, B. Bradlyn, T. K. Kim, T. Schmitt, C. Cacho, C. Felser, V. N. Strocov, and Y. Chen, *Nat. Phys.* **15**, 759 (2019).
- [42] H. Isobe and L. Fu, *Phys. Rev. B* **93**, 241113(R) (2016).
- [43] J. M. Link, I. Boettcher, and I. F. Herbut, *Phys. Rev. B* **101**, 184503 (2020).
- [44] I. Boettcher, *Phys. Rev. Lett.* **124**, 127602 (2020).
- [45] Y. Huang and S.-K. Jian, *Phys. Rev. B* **103**, L161113 (2021).
- [46] J. Z. S. Gao, X.-J. Gao, W.-Y. He, X. Y. Xu, T. K. Ng, and K. T. Law, *arXiv:2012.11287*.
- [47] X. Dai, Z. Fang, Y. Zhou, and F.-C. Zhang, *Phys. Rev. Lett.* **101**, 057008 (2008).

- [48] T. Nomoto, K. Hattori, and H. Ikeda, *Phys. Rev. B* **94**, 174513 (2016).
- [49] H. G. Suh, H. Menke, P. M. R. Brydon, C. Timm, A. Ramires, and D. F. Agterberg, *Phys. Rev. Research* **2**, 032023(R) (2020).
- [50] C. Setty, S. Bhattacharyya, Y. Cao, A. Kreisel, and P. J. Hirschfeld, *Nat. Commun.* **11**, 523 (2020).
- [51] See Supplemental Material at <http://link.aps.org/supplemental/10.1103/PhysRevB.104.L241115> for the details of the lattice and continuum models for RhSi, gap functions, generic DIII topological phases with the $s_+ \oplus s_-$ gap functions, nodal rings around R and their stability, and linearized gap equation, which includes Ref. [52].
- [52] C. Fang, M. J. Gilbert, X. Dai, and B. A. Bernevig, *Phys. Rev. Lett.* **108**, 266802 (2012).
- [53] H. Hu, J. Hou, F. Zhang, and C. Zhang, *Phys. Rev. Lett.* **120**, 240401 (2018).
- [54] I. C. Fulga and A. Stern, *Phys. Rev. B* **95**, 241116(R) (2017).
- [55] Y.-P. Lin and R. M. Nandkishore, *Phys. Rev. B* **97**, 134521 (2018).
- [56] H. Nielsen and M. Ninomiya, *Nucl. Phys. B* **185**, 20 (1981).
- [57] A. P. Schnyder, P. M. R. Brydon, and C. Timm, *Phys. Rev. B* **85**, 024522 (2012).
- [58] D. A. Pshenay-Severin, Y. V. Ivanov, A. A. Burkov, and A. T. Burkov, *J. Phys.: Condens. Matter* **30**, 135501 (2018).
- [59] A. P. Schnyder and S. Ryu, *Phys. Rev. B* **84**, 060504(R) (2011).
- [60] O. Vafek and A. V. Chubukov, *Phys. Rev. Lett.* **118**, 087003 (2017).
- [61] A. Chubukov, *Annu. Rev. Condens. Matter Phys.* **3**, 57 (2012).
- [62] A. Tsvyashchenko, V. Sidorov, A. Petrova, L. Fomicheva, I. Zibrov, and V. Dmitrienko, *J. Alloys Compd.* **686**, 431 (2016).
- [63] D. Salamatin, A. Tsvyashchenko, A. Salamatin, A. Velichkov, M. Magnitskaya, N. Chtchelkatchev, V. Sidorov, L. Fomicheva, M. Mikhin, M. Kozin, A. Nikolaev, I. Romashkina, and M. Budzynski, *J. Alloys Compd.* **850**, 156601 (2021).
- [64] B. Matthias, *J. Phys. Chem. Solids* **10**, 342 (1959).
- [65] D. J. Rebar, S. M. Birnbaum, J. Singleton, M. Khan, J. C. Ball, P. W. Adams, J. Y. Chan, D. P. Young, D. A. Browne, and J. F. DiTusa, *Phys. Rev. B* **99**, 094517 (2019).
- [66] R. Khasanov, R. Gupta, D. Das, A. Amon, A. Leithe-Jasper, and E. Svanidze, *Phys. Rev. Research* **2**, 023142 (2020).
- [67] R. Mizutani, Y. Okamoto, H. Nagaso, Y. Yamakawa, H. Takatsu, H. Kageyama, S. Kittaka, Y. Kono, T. Sakakibara, and K. Takenaka, *J. Phys. Soc. Jpn.* **88**, 093709 (2019).
- [68] Y. Okamoto, R. Mizutani, Y. Yamakawa, H. Takatsu, H. Kageyama, and K. Takenaka, *JPS Conf. Proc.* **29**, 011001 (2020).
- [69] K. Ishida, H. Mukuda, Y. Kitaoka, K. Asayama, Z. Mao, Y. Mori, and Y. Maeno, *Nature (London)* **396**, 658 (1998).
- [70] D. Mou, R. Jiang, V. Taufour, S. L. Bud'ko, P. C. Canfield, and A. Kaminski, *Phys. Rev. B* **91**, 214519 (2015).
- [71] S. B. Chung and S.-C. Zhang, *Phys. Rev. Lett.* **103**, 235301 (2009).
- [72] S. B. Chung, J. Horowitz, and X.-L. Qi, *Phys. Rev. B* **88**, 214514 (2013).
- [73] L. Chirolli and F. Guinea, *Phys. Rev. B* **99**, 014506 (2019).